Giuliano Agati[1]

Department of Mechanical and Aerospace
Engineering,
Sapienza University of Rome,
Via Eudossiana 18,
Rome 00184, Italy
e-mail: giuliano.agati@uniroma1.it

Alessio Castorrini

School of Engineering,
University of Basilicata,
Viale dell'Ateneo Lucano 10,
Potenza 85100, Italy
e-mail: alessio.castorrini@unibas.it

Francesca Di Gruttola

Department of Mechanical and Aerospace
Engineering,
Sapienza University of Rome,
Via Eudossiana 18,
Rome 00184, Italy
e-mail: francesca.digruttola@uniroma1.it

Serena Gabriele

Baker Hughes,
Viale F. Matteucci 2,
Florence 50127, Italy
e-mail: serena.gabriele@bakerhughes.com

Franco Rispoli

Department of Mechanical and Aerospace
Engineering,
Sapienza University of Rome,
Via Eudossiana 18,
Rome 00184, Italy
e-mail: franco.rispoli@uniroma1.it

Domenico Simone

Faculty of Aerospace Engineering,
University of Brasilia at Gama,
Brasilia 72444-240, Brazil
e-mail: domenico.simone@aerospace.unb.br

Paolo Venturini

Department of Mechanical and Aerospace
Engineering,
Sapienza University of Rome,
Via Eudossiana 18,
Rome 00184, Italy
e-mail: paolo.venturini@uniroma1.it

Domenico Borello

Department of Mechanical and Aerospace
Engineering,
Sapienza University of Rome,
Via Eudossiana 18,
Rome 00184, Italy
e-mail: domenico.borello@uniroma1.it

Numerical Prediction of Long-Term Droplet Erosion and Washing Efficiency of Axial Compressors Through the Use of a Discrete Mesh Morphing Approach

Online water washing represents an operation strategy commonly used to reduce compressor performance deterioration due to blade fouling. Since this kind of washing is applied when the machine operates close to full load conditions, injected droplets are strongly accelerated and consequently impact the rotor blades at high velocity, thus inducing undesirable phenomena like erosion. Here, we present a novel technique to study long-term water droplets erosion by also considering the geometry modification caused by droplets impacts. Two-phase unsteady numerical simulations were carried out, considering the injection of water droplets and their transport across the fluid flow in the first part of a real compressor, which is modeled in the region extending from the inlet to the rotor blades of the first stage. Simulations are performed on the whole machine to account for the asymmetric distribution of the spray injectors, the machine struts, inlet guide vanes (IGVs), and rotor blades. The $k-\varepsilon$ realizable turbulence model with standard wall functions was coupled with the discrete phase model to track injected droplets motion. Droplets-wall interaction is modeled following the Stanton–Rutland approach aiming at detecting the effect of droplet impact (deposit, rebound, and splashing) depending on the impact conditions. Moreover, a semi-empirical erosion model developed by the authors was used to evaluate the erosion induced by the droplets injection. Material removal due to erosion is converted into nodal mesh displacement that is used by a secondary routine to implement the mesh morphing scheme. The mesh modification is applied at discrete steps to reduce the computational load. This technique is adopted to account for the blades geometry modification due to water droplet erosion leading to performance losses. Moreover, an estimation of the compressor operating life before maintenance operations is given and the water washing efficiency during the whole life of the machine is evaluated by means of proper indices. At the end of the simulation workflow, erosion phenomena are observed in all the compressor regions, especially in the rotor where erosion peaks are reached at the hub of the blades leading edge. The rotor blades wet surface was found to remain almost constant at around 50% during compressor water washing. Erosive phenomena were proved to evolve nonlinearly with time indicating the need to account for the geometry modification for obtaining an accurate prediction of the long-time process.
[DOI: 10.1115/1.4055649]

Keywords: two-phase CFD simulations, water droplets erosion, mesh morphing, UDF, washing effectiveness, computational fluid dynamics (CFD), fluid dynamics and mass transfer phenomena in compressors

1 Introduction

The quest to keep turbine efficiency as high as possible over time is considered mandatory by manufacturers and plant managers. High efficiencies limit fuel consumption, thus reducing operational costs, as well as the environmental impact of gas turbine engines.

Blade fouling is one of the most important reasons for performance degradation due to strong increase in pressure losses [1–3]. It is common to use water washing techniques to remove deposits from compressor blades, thus maintaining high efficiency. Water washing can be performed offline and online, with the latter being used to avoid production stops as well as large performance degradation between two offline washings. The importance of online compressors water washing was discussed in several studies available in the open literature. In Ref. [4], the authors showed that the washing efficiency increases when increasing the water wash rate, keeping the compressor efficiency constant, and close to the maximum value, thus reducing fuel consumption. A life cycle assessment study [5] demonstrated the feasibility of this solution despite the duties related to freshwater availability, heating, and pumping. Abgadede et al. [6] studied the influence of droplet size on compressor water washing by estimating its efficiency before and after the washing procedure. They found that the injection of larger droplets leads to a better recovery of power losses due to compressor fouling. A parametric study of an online aero engine washing system was performed in Ref. [7], varying the inlet pressure and size of droplets. Baikov et al. [8] studied the effectiveness of a detergent solution composed of a mixture of aqueous Ammonia and Trilon B, in dissolving deposits on the axial-compressor blades of a gas turbine engine. In Ref. [9], compressor cleaning by adoption of two-phase detergent mixtures was tested in both laboratory and on-field tests. The authors found that two-phase solutions provide a better washing efficiency in comparison with single-phase solutions. Igie et al. [10] investigated the impact of offline and online compressors washing by analyzing machine-generated data. Four different gas turbine engines were examined. Different washing frequencies, liquid concentrations, and washing types (offline and online) were studied aiming at quantifying the respective effect on the engine performance. Wang et al. [11] studied the effect of slope angle of the compressor wall on the splash condition of washing droplets, with the aim of optimizing the water injection system. Musa et al. [12] computed the economic viability of the online washing process of axial compressors. The authors performed a cost-benefit analysis for several gas turbine engines and rated capacities, ranging from few megawatt power up to 300 MW units, finding that larger engines have a higher return on investment in comparison to the smaller units.

The increasing use of online washing raises the need to understand what happens to the compressor blades when, rotating at their nominal velocity, are hit by water droplets with high relative velocity. Indeed, during online water washing, the compressor speed is almost constant [13], thus maintaining the engine close to the design conditions. This means that water droplets hit the blades at very high-speeds, which may cause erosion of the compressor blades [14]. To study the effect of water droplet erosion (WDE) in Ref. [15], we developed an erosion model based on experiments available in the open literature [16,17]. The WDE model was applied to several compressor blade geometries in the past [15,18–21]. In all these simulations, the computation of the erosion mechanism was carried out by assuming that the profile did not change due to the erosion itself thus neglecting the variation in the fluid flow due to the profile modification. This is a very convenient approach as the fluid flow field has to be computed just once and the "frozen" fluid flow can be used to calculate droplet trajectories. However, WDE is a long-time process. During the machine operating life, the compressor blades are eroded thus continuously changing their geometry. Therefore, during the erosion process, the flow field might change as well increasing profile losses. So, the design geometry can be used only to simulate the beginning of the erosion process, when erosion of the target geometry is negligible. However, for more accurate predictions, considering the whole compressor lifetime, and to study whether and how the process varies in time, the target geometry should change according to the erosion process. This issue is present in several turbomachinery applications. For instance, in simulating deposit build-up in gas turbine cooling passages, Bowen et al. [22] accounted for geometry modifications by re-meshing the domain at each particle deposition. The same approach is adopted in Ref. [23] to simulate particle deposition on gas turbine blades. In Ref. [24], a compressor erosion analysis was coupled with a structural analysis of the compressor blades. However, the computational cost associated with this approach is too high and not affordable in industrial applications where large domains must be simulated. Furthermore, the erosion process is quite slow and a continuous update of the geometry will lead to minimal updates of the geometry at any time-step with negligible prediction improvements.

Aiming at simulating long-time (erosion/fouling) processes in industrial applications, in 2016 we started developing and optimizing an algorithm to perform long-term predictions with a reduced computational time [24–28]. In the present paper, this algorithm is tailored for predicting the WDE process in a whole rotating compressor, from the inlet to the first-stage rotor. In the following
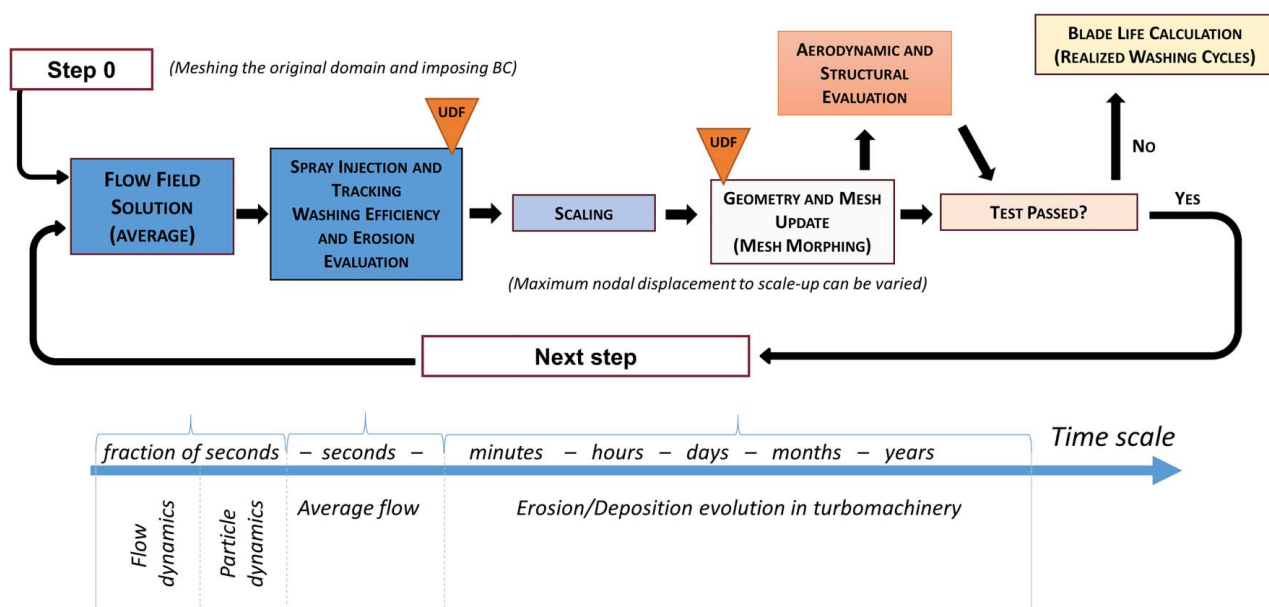

Fig. 1 Simulations workflow to evaluate the long-term erosion process and time scales of the involved physical phenomena. (© 2022 Baker Hughes Company–All rights reserved.)

section, we describe the rationale of the erosion algorithm coupled with a mesh morphing scheme used for the blades surface modification during the process. Then, numerical details about the present application are reported. In Sec. 4, we show and discuss the results. Some final remarks and conclusions close the paper.

2 Models and Methodology

A scheme of the workflow used to simulate the whole washing/erosion process is reported in Fig. 1 along with a time scale of the involved physical phenomena. As a first step, we solve the flow field in the design geometry (see Sec. 2.1) and, as soon as the simulation stabilizes and reaches convergence conditions, water sprays are injected (Sec. 2.2). Whenever a droplet hits a surface the erosion is computed runtime, and, at the end of the simulation (i.e., when all the droplets deposited or left the domain), results are used to evaluate the erosion patterns and water washing indices (see Sec. 2.3). Since the domain geometry varies with time, the considered grid (and hence the flow field and droplet dynamics) should change accordingly. In the present paper, this is done by adopting proper scale factors (Sec. 2.4) at the end of each simulation (thus representing an erosion evolution step).

There is a crucial aspect that should be considered when generating the updated grid. The generation of the proper computational mesh for complex geometries and high Reynolds numbers as occurring in compressor stages is a difficult and time-consuming procedure. On the other side, the erosion mechanism interests just a small fraction of the overall domain, and the total accepted erosion cannot be greater than few (or, as in the present case, a fraction of) millimeters. Therefore, to avoid re-meshing the whole domain after each erosive impact, a moving mesh approach is here used. For such a procedure, we rely on the dynamic mesh tool built in FLUENT to move the internal mesh nodes according to the boundary modification computed using user defined functions (UDFs) developed on purpose. Here, the dynamic mesh tool has been configured to smoothing mode only, selecting the linear elastic solid method [29]. This method treats the grid as an equivalent elastic solid, maintaining the quality of the cells by the application of volume stiffness. The parameters used for this application are: 0.45 Poisson's ratio, 50 as the number of maximum iterations, and the smoothing applied from the last updated configuration.

As explained in Ref. [24], at each evolution step the eroded geometry needs to be examined from both a structural and aerodynamics point of view. If both the tests are passed (as we assume in the present paper), we reset the variables used during the simulation in the UDFs, and the simulation cycle (namely a new evolution step) starts again. If one of the above tests is not passed or if the erosion reaches the maximum permissible value, the simulation cycle stops and the blade life (namely the amount of water needed to provoke the threshold erosion thickness) is computed. In Ref. [28], the capability of the proposed approach to accurately predict the long-time erosion process was validated by comparing simulations with experimental measurements (Fig. 2) performed at the Department of Mechanical and Aerospace Engineering (Sapienza University of Rome) Laboratory, Rome, Italy. Despite in Ref. [28], the methodology was applied for solid particle erosion, the scaling integrated procedure is the same, showing the reliability of the adopted approach.

2.1 Flow Field. The process of mesh morphing due to particle collisions on the walls of struts, IGVs, and first-stage rotor of an axial compressor is numerically investigated. Here, the rotor is considered in a rotating configuration at design conditions, representing online water washing. The simulations are carried out by using ANSYS FLUENT 2020R2. Turbulence of the carrier phase is modeled by solving unsteady Reynolds averaged Navier–Stokes (U-RANS) equations and employing the well-established, widely accepted k–ϵ realizable model [29]. Near the walls, the widely used, universally accepted standard wall function, based on the Launder and Spalding approach [30], is adopted. The governing equations are solved using the coupled pressure-based solver algorithm. The SIMPLEC solution method was selected for the pressure-velocity coupling. The pressure is discretized spatially by the second-order upwind scheme, while for all the other variables a first-order scheme is adopted. The time advancement assumes a time-step equal to 3.0×10^{-5} s, while the integration of droplets motion is achieved by an automated tracking scheme that permits switching between a numerically stable implicit low order scheme and a trapezoidal higher order one. Moreover, the accuracy control option permits the solution of droplets equation of motion to be within a tolerance of 1.0×10^{-5}.

The flow in each moving cell zone is solved using the moving reference frame or the so-called "frozen rotor" approach. This means the freezing of the moving rotor in a specific position and the observing of the instantaneous flow field in that condition for the whole computation [29]. The rotor cell zone rotates with an angular velocity $\omega = -7800$ rpm. However, to guarantee the reaching of a convergent steady solution, the solution process was based on a gradual increase of the angular velocity. Thus, first, a $\omega = -4800$ rpm was imposed to the rotor cell zone and only after reaching a stable solution, rotational speed was increased up to the design value.

2.2 Dispersed Phase. The dispersed phase is modeled by the discrete phase model, based on Eulerian–Lagrangian one-way coupling approach, meaning that mutual interaction between the two phases (carrier flow and droplets) is not accounted for. An earlier simulation was performed by also considering the mutual interaction between the two phases (i.e., two-way coupling), since in the proximity of the injection points droplets volume fraction can reach high values. However, the difference in the results of the washing process (in terms of washing efficiency and induced erosion) was not relevant. This might be motivated by considering that the second phase volume fraction reaches values within the range of the two-way coupling regimes only at the inlet section of
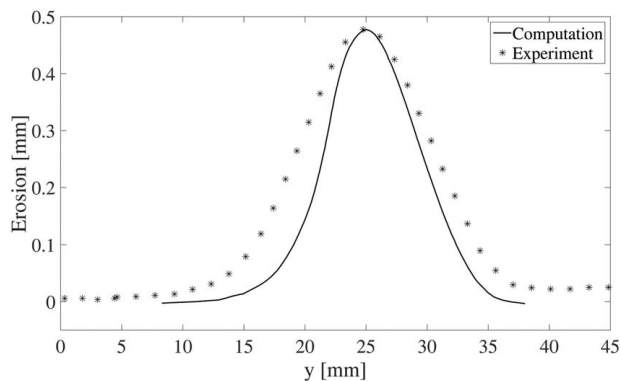

Fig. 2 Comparison of numerical prediction and experiments of long-term erosion process on an aluminum specimen (data from Ref. [28])
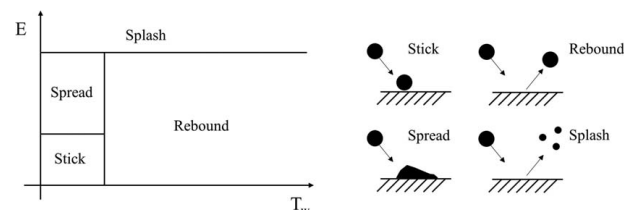

Fig. 3 Different droplet impact regimes identified by the adopted model [19]

the compressor. Droplets are quickly dragged through the domain, and, because of the different injection positions, each cloud of droplets follows different patterns resulting in low values of the volume fraction in most of the numerical domains. Droplets are all injected for two time-steps and tracked up to their destination, which may be the exit from the fluid domain or the deposition on a solid surface.

Droplet impact on a solid surface is an extremely complex phenomenon and its physical explanation can be largely different depending on the impact conditions. The authors refer to the reviews by Yarin [31], and Joressand and Thoroddsen [32] for a comprehensive understanding of the phenomenon. In the present work, the Stanton–Rutland model [33], extended using the concepts from O'Rourke and Amsden [34], is adopted to predict the outcome of a droplet impact on a wall. In this model, four different impact regimes are considered for a drop-wall interaction according to local impact conditions (i.e., local wall temperature and a parameter E linked to the impact velocity [34] defined in the next paragraph). These regimes can be sticking, spreading, splashing, or rebounding as illustrated in Fig. 3.

Mundo et al. [35] performed experiments on the impact of droplets on dry surfaces and found a splashing criterion, based on a dimensionless parameter related to the drop Reynolds number and the Ohensorge number. In Ref. [34], this criterion was extended to take into account the possible presence of a water film on the wall. The authors proposed to use a splash Mach number (E) based on the impact velocity and the capillary wave speed of a wave of length D

$$E = \frac{v}{\frac{1}{D}\sqrt{\frac{\sigma h_0}{\rho}}} \qquad (1)$$

where v is the droplet impact velocity, h_0 is the initial film thickness, and σ and ρ are the liquid surface tension and density, respectively. The splashing criterion identified in Ref. [33] reads

$$E^2 = \frac{\rho v^2 D}{\sigma} \frac{1}{\min\left(\frac{h_0}{D}, 1\right) + \frac{\delta_{bl}}{D}} > (57.7)^2 \qquad (2)$$

which is equal to the criterion identified in Ref. [34] for $h_0 = 0$ and it reproduces the physical observed trend: if a liquid film is present at the impact location, splash is suppressed since the impact energy is radiated through capillary waves and viscous damping effects become relevant. In Eq. (2), δ_{bl} is a boundary layer thickness, defined by

$$\delta_{bl} = \frac{d}{\text{Re}} \qquad (3)$$

where the drop Reynolds number is based on the impact normal velocity and on the droplet diameter d. A droplet rebound occurs when the impact energy is low and the wall temperature is larger than a critical value T_{crit}, which is linked to the saturation temperature of the liquid droplets. In the present configuration, wall temperature is always lower than the T_{crit}, so droplets can only stick, spread, or splash depending on the impact energy. The transition criteria for the rebounding regime based on the Weber number is $5 < \text{We} < 10$. If the impact energy is low, the droplet can deposit on the surface creating a liquid film. The sticking criterion, based on experimental observations, is $\text{We} < 5$ [33]. Spreading is similar to the sticking regime but occurs at higher We.

If the energy is large enough to overcome the splashing threshold (Eq. (2)), the droplet will rebound forming secondary smaller droplets that may impact and erode other solid surfaces. The obtained secondary droplet diameters are sampled by a cumulative probability Weibull distribution function that was fitted to the experimental

data from Mundo et al. [35]

$$f(d) = 2\frac{d}{D^2}\exp\left[-\left(\frac{d}{D}\right)^2\right] \qquad (4)$$

which indicates the probability to find drops of size d_i in a sample of splashed droplets. Distribution limiting method is also used to avoid unphysical too large droplets. In the adopted solver, it is possible to set the number of secondary droplets generated due to a splashing impact. In this work, because of the large extension of the domain and the large number of injected parcels, to not make the computation too resources consuming, this number was set equal to 2. Nevertheless, this parameter affects only the number of particles per parcel and not the splashed droplets mass. In fact, the mass fraction, i.e., the ratio between the splashed mass and the impacting mass, follows the expression given by O'Rourke and Amsden [34] fitting the experimental data by Yarin and Weiss [36]. To compute secondary droplets trajectories, normal and tangential components of velocity need to be defined. The normal component of velocity is calculated by sampling a cumulative probability distribution function obtained from a Weibull distribution function that was fitted to the experimental data from Mundo et al. [35]. The tangential component of the rebound velocity is computed from the normal component velocity given an expression for the reflection angle.

In the present work, the wall film is not modeled in an Eulerian framework, i.e., no equations for the thin liquid film dynamics are solved. This means that once a droplet deposits on a surface, it creates a liquid wall film that does not move. This aspect will be analyzed in future works. However, the Stanton–Rutland model can predict the film formation since, for low impact energy, droplets impact can result in a deposit ("stick") of the dispersed phase. Every time a droplet hits a solid surface, a UDF developed by the authors [19] and containing the WDE model presented in Refs. [15,18], is activated. The erosion model was developed for stainless steel targets and it is based on the experiments reported in Refs. [16,17]. It accounts for all the main quantities affecting the erosion process (i.e., impact velocity and angle, droplet size, material properties of both droplets and target surface, surface roughness and hardness, and incubation period). It allows access to several useful pieces of information to study the major aspects of the erosion phenomenon that are relevant in the present case.

As widely accepted in the literature, WDE process can be divided into three main steps (Fig. 4). In the beginning, droplets hitting the target discharge part of their energy on it without removing material. This energy accumulates until a threshold value is reached after which removal of material occurs. This is called "incubation" period. Once the erosion starts on a target surface, any new droplets hitting the same surface will remove some material with an erosion rate that is the maximum measured on that surface. This *transition* period goes on until the second threshold energy is overcome. After that, a *stationary* period starts, erosion rate decreases to a steady
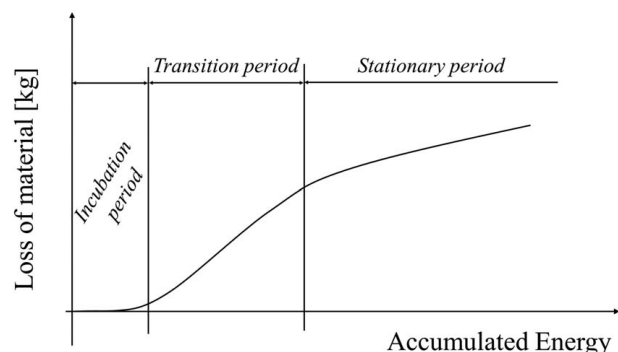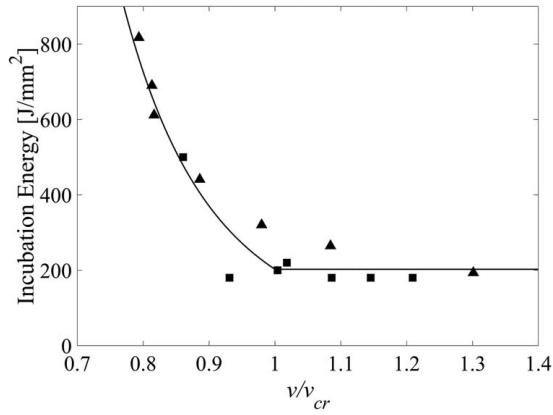

Fig. 4 Erosion curve as a function of the accumulated energy

Fig. 5 Incubation energy as a function of the impact-to-critical velocity ratio. Experimental data (squares [16], triangles [17]) and proposed fitting curve [15].

Table 1 Values of the constants used for stainless steel [36]

a	b	γ	k	$\dot{m}_{ref}$	v_{ref}	d_{ref}
5,1	2	~0.0048	2.0746	0.01743	568	30.6

value where the erosion process progresses. From the experiments in Refs. [16,17], the incubation period (converted into "incubation energy" that is the impact energy per unit of the target surface that has to be accumulated before erosion takes place) can be expressed as a function of the impact velocity. This is true up to a critical velocity (depending on the droplet size) above which the incubation energy is almost constant (about 200 J/mm^2 in the case of stainless steel). According to the experiments, it was possible to extract an algebraic relation as follows:

$$v_{cr}(d) = -0.18446d + 433.47117 \qquad (5)$$

where v_{cr} is expressed in m/s, while d is expressed in μm. If the impact velocity of a droplet is smaller than v_{cr}, the incubation energy of the target increases readily.

Once the critical velocity is known, the incubation energy (E_{inc}) can be written as a function of the ratio between the actual impact velocity and the critical velocity for the considered droplet size, $v/v_{cr}(d)$ (Fig. 5)

$$E_{inc}(v, d) = \begin{cases} 202.55\left(\dfrac{v}{v_{cr}(d)}\right)^{-c} & \text{for} \quad \dfrac{v}{v_{cr}(d)} < 1.0 \\ 202.55 & \text{for} \quad \dfrac{v}{v_{cr}(d)} \geq 1.0 \end{cases} \qquad (6)$$

where $c = 5.723$.
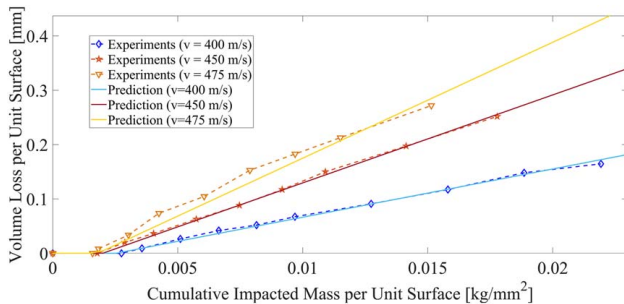
Fig. 6 Comparison of model prediction and Kirols' experiments for droplets with a diameter equal to 220 μm [15]

The effect of the initial roughness of the target surface on the incubation energy, discussed in Ref. [16], is considered in the model by introducing a roughness coefficient C_r, that is the ratio between the incubation energy with a certain roughness and the incubation energy E_{inc} in the reference case (Ra$_{ref}$ = 0.2 μm [16]).

Hence

$$E_{inc} = E_{inc}(v, d)C_r(\text{Ra}) \qquad (7)$$

with C_r defined as

$$C_r = \frac{E_{inc}(\text{Ra})}{E_{inc}(\text{Ra}_{ref})} = 0.66436401\text{Ra}^{-0.254079426} \qquad (8)$$

Lee et al. [37] model was adopted to account for the effect of the surface hardness (H) on the erosion rate (ER)

$$\text{ER} = \left(\frac{k}{\dot{m}_{ref}}\right)\left(\frac{v}{v_{ref}}\right)^a\left(\frac{d}{d_{ref}}\right)^b 10^{g\text{Hv}} \qquad (9)$$

ER is expressed in cubic millimeters (of removed material) per impacting kilogram of water. $\dot{m}_{ref}$, v_{ref}, d_{ref}, and a are constants independent from the material properties, while k, b, and g are constants dependent on the material. Hv is the Vikers hardness of the target surface. These quantities are summarized in Table 1 for stainless steel.

Last, the effect of impact angle is accounted for by considering only the normal components of the impact velocity, according to the findings of Ahmad et al. [38]. Figure 6 shows the comparison between experiments in Ref. [16] and the model prediction. Further details about the erosion model can be found in Refs. [15,18].

2.3 Water Washing Indices. It is not easy to estimate the water washing efficiency (WWE) since it depends on several factors, such as the capability of the injection system to reach the desired surfaces and the ability of liquid to dissolve deposited dirt, which, in turn, is strongly affected by the amount of water hitting a given surface and by the impact conditions. Despite some of these factors can be hardly summarized by a single scalar quantity in Refs. [18,19], we introduced some indices for evaluating the WWE. Here, we modified those indices in the attempt to better represent the WWE.

Wet-to-Total Surface (WTS): It is the ratio between wet and total surfaces. It measures the fraction of a surface hit by water droplets. A larger WTS may result in a higher WWE.

Local Impacted water mass Fraction (LIF): This quantity represents the fraction of water mass hitting a specific surface with respect to the total impacted mass. It indicates the capability of the washing system to wash the compressor surfaces: the larger the LIF on the rotor, the larger WWE is supposed to be.

Normalized impacted water mass per unit of wet surface (IMWS): This is the normalized ratio between the total impacted water mass on all the rotor blades and the maximum wet surface. Keeping the other quantities constant, the larger the IMWS, the better the system is supposed to wash.

2.4 Scale Factors. First, we have to point out that the real injection period is relatively long (years) while the time interval used for the computations is obviously small due to the limitations related to computational issues of the grid and the high velocities involved. It is then important to properly reproduce the injection mechanism, but at the same time, to compute the long-term effect of water injection on washing and erosion mechanisms, a scaling process is needed. This concept can be well understood by observing the time scale of the involved physical phenomena reproduced in Fig. 1. In the present simulations, two scale factors (introduced in the following paragraphs) are used.

A first scale factor (F_1) is introduced to speed up the process and start the erosion at least on some of the domain walls. Hence, given
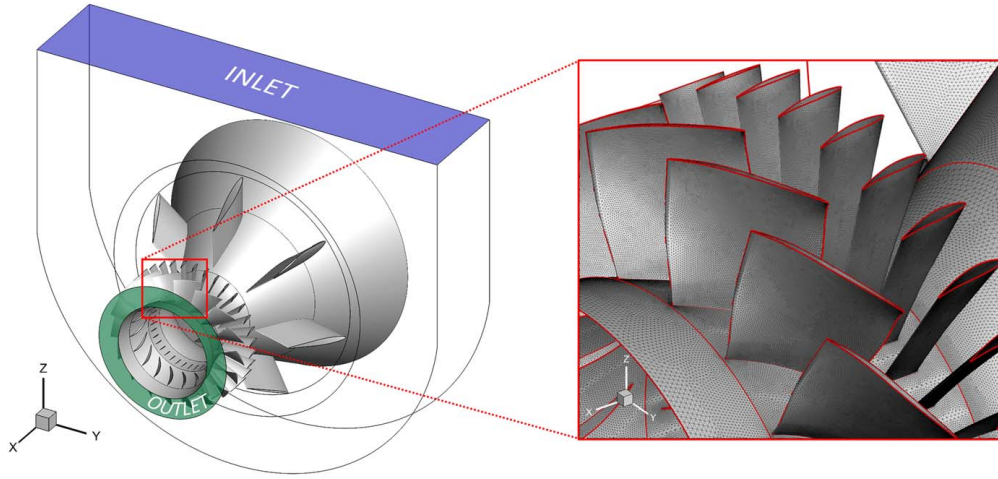
Fig. 7   Numerical domain (left) and zoom-in of the first-stage rotor (right). (© 2022 Baker Hughes Company–All rights reserved.)

the injector mass flow rate, the amount of simulated water mass ($m_{inj,sim}$) is multiplied by F_1. Therefore, the use of F_1 fictitiously increases the simulated time and water mass: each droplet represents F_1 droplets. The factor F_1 is always the same for all the evolution steps. By knowing both the real and fictitious water flows, the time needed to reach the incubation energy on each surface can be easily estimated. Indeed, until erosion does not start, domain geometry remains the same, as well as the flow field and particle dynamics.

As soon as the accumulated energy overcomes the incubation energy, erosion takes place and, thanks to the erosion model implemented in the UDF, the performed simulations allow us to calculate the amount of material removed from the target surface. At the end of each simulation, a second scale factor (F_2) is needed. In fact, theoretically, once the erosion starts on a wall cell, each impact on that grid cell would provoke a geometry modification. However, we can assume that until the thickness of the eroded material is smaller than a threshold value e_{thr}, the effect of geometry variation on the flow field is negligible. If the flow field does not change, we can assume that also the dispersed phase will globally have a similar behavior. Thus, until the thickness of the eroded material is smaller than e_{thr} nothing is changing in the simulation and the erosion rate remains constant. Generalizing this concept, at the end of the simulation of the nth evolution step we want the global maximum erosion to be equal to $e_{thr} \cdot n$; therefore, the simulated erosion, which in general differs from this value, has to be scaled accordingly.

Indicating with $\{X_n\}$, $\{x_n\}$, and F_n respectively the scaled node displacements, the non-scaled node displacements, and global scale factor (introduced only for mathematical passages) at the end of the evolution step n for every grid node it writes

$$\{X_n\} = F_n \sum_{i=1}^{n} \{x_i\} - \sum_{i=1}^{n-1} \{X_i\} \qquad (10)$$

This means that for the nth *step,* the scaled displacement vector of all the mesh nodes, with respect to their previous position at the step $n-1$, is equal to the displacement due to erosion computed by the simulation $\{x_n\}$ multiplied by the global scaling factor F_n.

To compute the scaling factor $F_{2,n}$, we must consider that at the point of maximum erosion (P) at the end of the evolution step n should result

$$F_{2,n} \sum_{i=1}^{n} \{x_i\} = e_{thr} n \qquad (11)$$

and that

$$\{X_n^P\} = \{x_n^P\} F_{2,n} \qquad (12)$$

By writing Eq. (10) in the point (P), we can compute the scaling factor

$$F_{2,n} = \frac{e_{thr} n - \sum_{i=1}^{n-1} \{X_n^P\}}{\{x_n^P\}} \qquad (13)$$

By multiplying, at the end of each nth simulation, all the non-scaled node displacements by $F_{2,n}$, we ensure to reach in one point only of the rotor the threshold value of $e_{thr} \cdot n$, while all the other rotor scaled node displacements will be smaller. To find the point (P), the scale factor $F_{2,n}$ is computed in all the rotor grid nodes, the lowest value of $F_{2,n}$ will be the selected one.

Knowing $F_{2,n}$, we can evaluate the water mass flow needed to provoke the erosion reached at the end of the nth evolution step, as $F_1 m_{inj,sim} F_{2,n}$.

As explained above, the series of simulations stops when the maximum permissible erosion in the rotor region e_{stop} is reached. The global actual operating time needed to reach e_{stop} (namely the blade life), can be calculated knowing the actual water mass m_{stop} needed to provoke e_{stop}

$$m_{stop} = F_1 \sum_{i=1}^{n} m_{(inj,sim)} F_{(2,i)} \qquad (14)$$

Then, knowing the real water mass m_{stop}, the washing frequency and duration, and the blade life can be estimated.

3   Computational Details

3.1   Computational Domain and Mesh. In the present study, the computational domain reproduces the inlet section of a real axial compressor up to the first-stage rotor. The whole machine and not only a sector is here simulated. This is necessary to consider the asymmetrical distribution of the water droplets injectors and the non-commensurable ratio among struts, IGV, and rotor blades. Because of the high rotational velocity imposed on the rotor, the idea of considering a moving mesh approach is unrealistic. For this reason, a frozen rotor approach was selected to account for the machine rotation.

The mesh is composed of around 26 M tetrahedral cells, clustered in the wall regions to guarantee values of $y+$ ranging from 20 to 300 (the reader can refer to Ref. [20] for further details). Such range represents the interval of applicability of the standard wall function and guarantees that the near-wall turbulence is correctly solved in the framework of the adopted models. An overall view of the computational domain is shown in Fig. 7 together with a blow-up of the computational mesh in the rotor region.
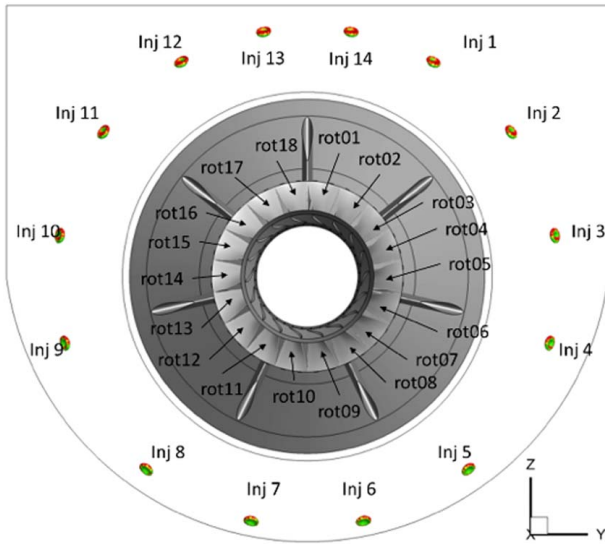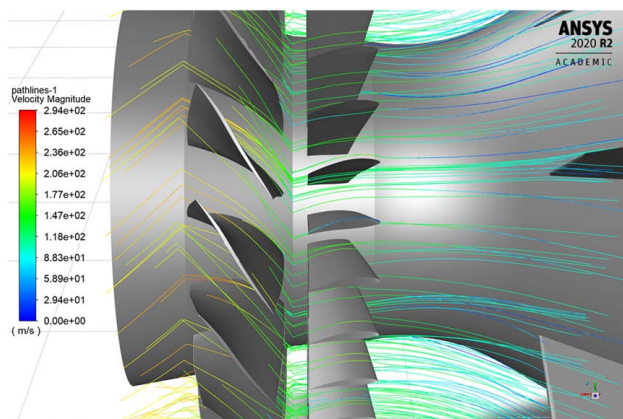
Fig. 8 Position of the injectors and rotor blades [21]. (© 2022 Baker Hughes Company–All rights reserved.)
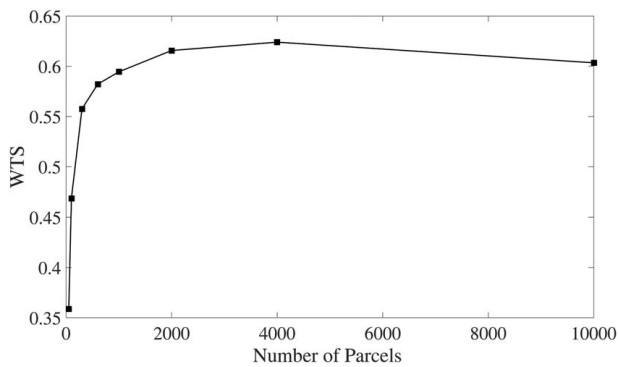
Fig. 9 WTS variation as a function of the number of parcels

To prevent IGVs from shadowing the rotor blades, so affecting the erosion patterns, the present grid was built in such a way that rotor blades leading edge is located in a circumferential position corresponding to the mid-pitch between two successive IGVs (see also Fig. 10). In Ref. [20], simulations were also performed on a different geometry in which rotor blades leading edges (LE) were placed in the wake released by IGVs trailing edge. The reason we selected the present configuration is that here erosion resulted more pronounced.
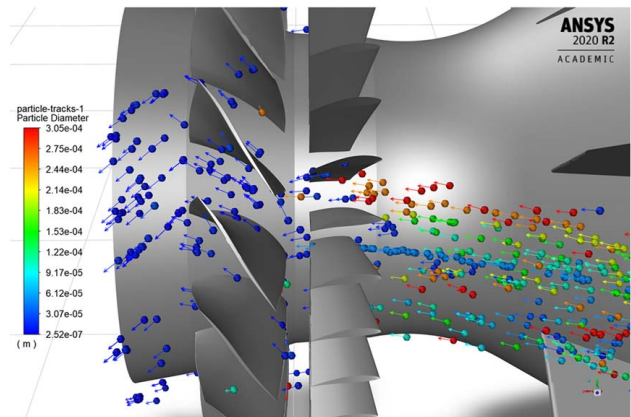
3.2 Evolution Steps. To simulate long-time erosion, simulations are divided into "evolution steps". As reported in Fig. 1, each evolution step is composed of: a steady simulation of the flow field only, a transient droplets injection and tracking within the domain, and impacts and erosion computations. At the end of an evolution step, we apply the scaling procedure described in Sec. 2.4 and perform a mesh morphing to update the geometry. The new geometry should be checked from a structural and aerodynamic point of view (this part is not included in the present paper), and if the test is passed a new evolution step starts. This process is repeated until the maximum level of erosion allowed in a rotor point is reached. In the present simulation, this latter quantity is assumed equal to 0.3 mm, with the maximum thickness per evolution step equal to 0.1 mm. Thus, in the present simulation, three evolution steps are simulated in total.

3.3 Carrier and Discrete Phases Boundary Conditions. The airflow enters the domain from the upper surface of the inlet compressor region and exits from the outlet section (Fig. 7). A mass flow boundary condition (BC) is used for the inlet; the air mass flowrate here considered is the nominal one for the simulated compressor. For the outlet, a pressure outlet BC is adopted. The value of the pressure at the outlet was obtained by calculating the Eulerian work exerted by the rotor to the fluid and compared with the industrial design value. All the other surfaces are treated as no slip adiabatic walls.

As already reported, a frozen rotor approach is adopted to model the rotation of the machine. For this purpose, a rotation $\omega = 7800$ rpm with respect to the negative x-axis was set for the rotor cell zone. The rotating components (the rotor lower wall and the rotor blades) are set as rotating walls with null angular velocity in the relative frame of reference while for the upper casing (not shown in Fig. 7) a positive angular velocity $\omega = 7800$ rpm was set.

Water droplets are injected through 14 nozzles circumferentially distributed along the inlet section of the domain as illustrated in Fig. 8 (Inj1–Inj14), where also the rotor blades IDs are listed (rot01–rot18). For this purpose, the "full cone injector" (solid cone injector, as named in ANSYS FLUENT [29]) was selected as the most appropriate to reproduce real injection conditions. Droplet size classes to be simulated have been provided by experiments, ranging from few micrometers up to about 400 μm. However, to speed up the simulations we considered the size classes containing most of the mass (namely the 80% of the total injected mass). We simulated six size classes ranging between 50 μm and 305 μm.

An important aspect needing attention is the statistical relevance of the obtained results. Indeed, for those size classes containing a small number of droplets, a single simulation could result in an extreme localization of the impacts, thus affecting the whole

Fig. 10 Streamlines in the IGV-rotor region colored by velocity magnitude. (© 2022 Baker Hughes Company–All rights reserved.)

Fig. 11 Some droplets in the IGV-rotor region are colored by their size. Vectors indicate droplet velocity. (© 2022 Baker Hughes Company–All rights reserved.)
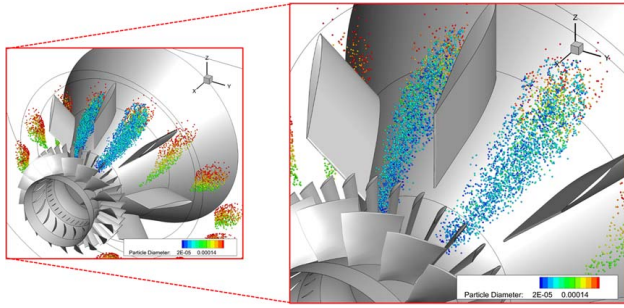
Fig. 12 Snapshot of one of the performed simulations capturing the splashing phenomenon of some droplets occurring on the internal upper cone of the compressor [19]. (© 2022 Baker Hughes Company–All rights reserved.)

simulation. Therefore, even though one has to increase the number of simulated droplets to reach a statistical independence of the results, on the other hand, increasing the number of droplets results in a larger computational time. This limit can be bypassed properly selecting ANSYS FLUENT for the number of parcels representing each size class. Indeed, each size class is simulated by several parcels, each containing a fraction of the whole mass. A parcel behaves like a droplet from the dynamics point of view, but some quantities (i.e., the impact energy) are proportional to the transported mass. According to the findings in a simplified geometry, varying the number of parcels (Fig. 9) an asymptotic behavior on WTS index is observed starting from the 600 parcels case. Therefore, in the present study, 1000 parcels per size class per injector are simulated. Considering that for each simulation we inject water for two time-steps, that the washing system design is composed of 14 injectors, and that we simulate three evolution steps, we are distributing the total injected mass in 504,000 parcels, a

number which is large enough to have statistically meaningful results.

4 Results and Discussion

4.1 Flow Field and Droplet Dynamics. The details of the flow field are reported in earlier papers published by the authors [20,39]. For this work purpose, we report two figures representing the main features of the flow field (Fig. 10) and of the droplet dynamics when reaching the rotor stage (Fig. 11). As expected, the flow is deviated and accelerated, reaching high velocities (about 300.0 m/s).

In Fig. 10, streamlines in the rotor region are traced in the relative reference frame. A snapshot of some droplets entering the rotor region is reported in Fig. 11 along with their velocity vectors. It is worth noticing that most of the depicted droplets are in the smaller size class. This is related to the impacts occurring upstream, in the inlet case region. As shown in Fig. 12, a large number of the injected droplets impact the inlet cone, splash and are nebulized into smaller droplets, which go washing the IGVs and the rotor region.

4.2 Time Evolution of Erosion. In Fig. 13, the magnitude of the cumulative erosion induced on the upper part of the domain is shown at the end of the simulation workflow, here considered as the end of the compressor life. In addition, in Fig. 14, the total erosion on the lower part of the domain is presented for the same erosion evolution step. The erosion patterns depict the cumulative erosion experienced by the machine on the three steps in which its working life was divided as explained in Sec. 2.4. In both the top and bottom parts of the machine, large regions subject to water droplets erosion are visible. A pronounced erosion is evident on the internal cone and on struts, which present erosion both on their leading edges and on the lateral sides. The same can be said for all the IGVs. In general, no
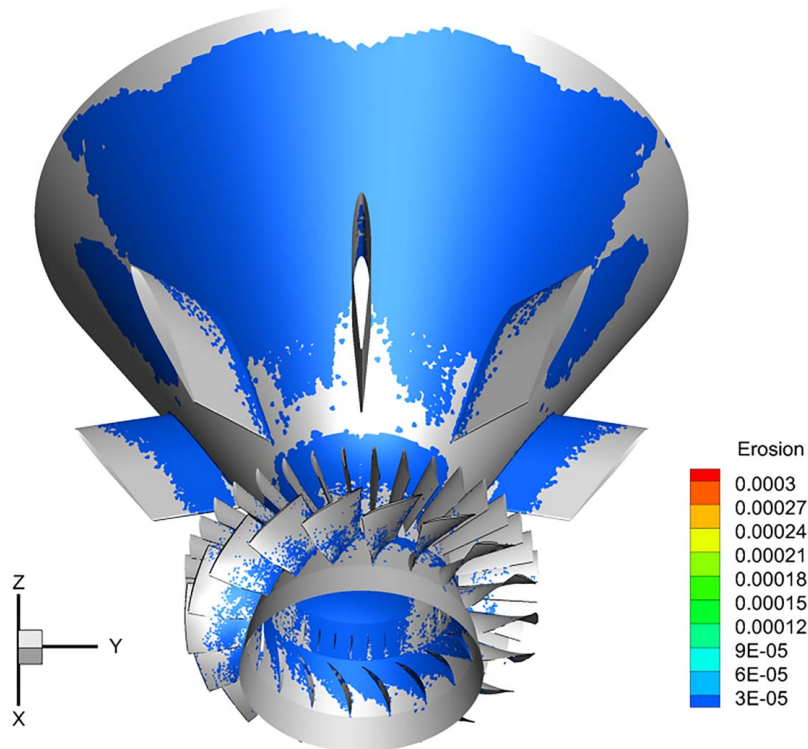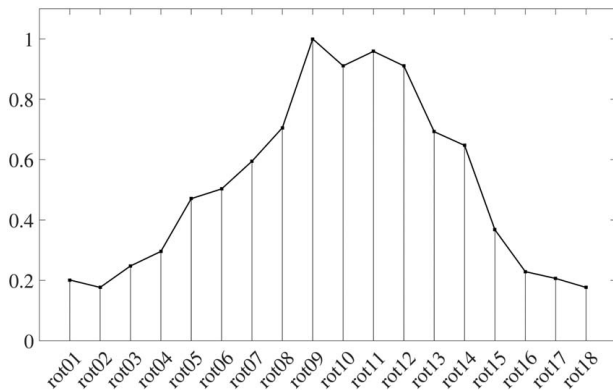

Fig. 13 Front view of the erosion induced on the upper part of the axial compressor at the end of the simulations process performed. (© 2022 Baker Hughes Company–All rights reserved.)
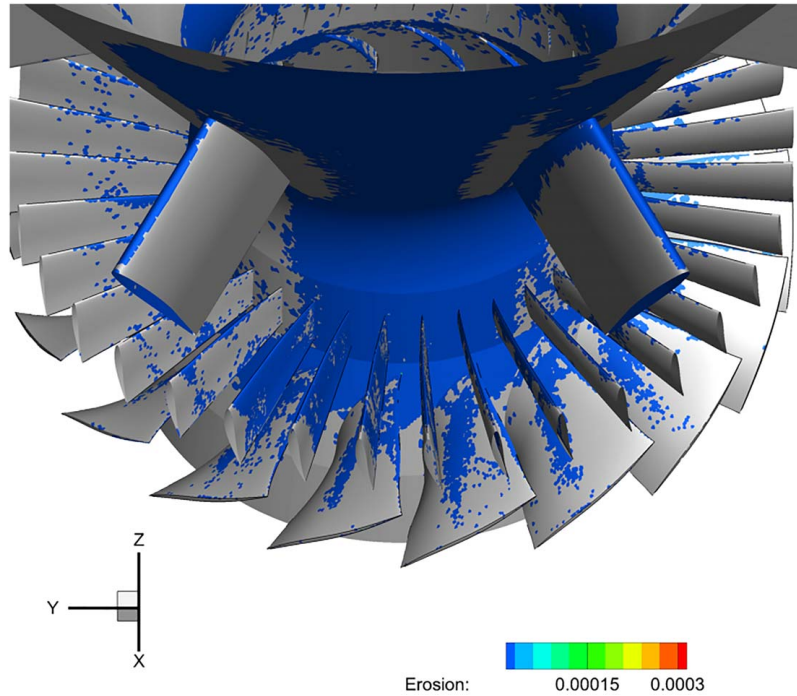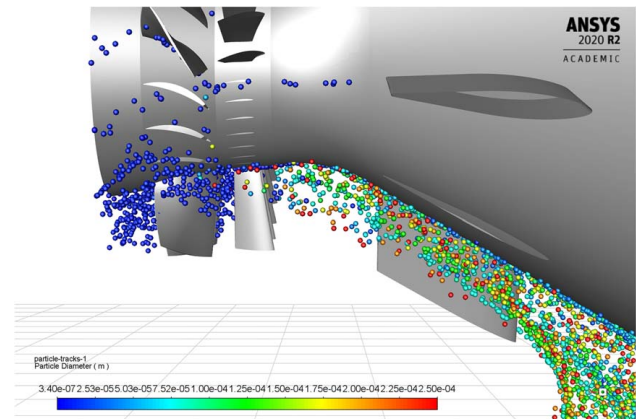
**Fig. 14 Back view of the total erosion induced on the bottom part of the axial compressor after the third droplets injection. **

**Fig. 15 Normalized accumulated energy due to droplets impacts on the rotor blades. The quantity is averaged among the three mesh evolution steps here considered. **

**Fig. 16 Dispersed phase distribution when entering the rotor. Droplets are colored with their size. **

symmetric erosion profiles are noticed, due to the not staggered distribution of the injectors as shown in Fig. 8. Unfortunately, in the presented contour plots, it is not evident the variation of the erosion in most of the domains. This is because the peak of the erosion of 0.3 mm is located on a single grid point on one of the rotor blades while all the other values of erosion are smaller. Also at the inlet of the machine, before reaching the rotor region, erosion peaks are observed on the lower part of the internal cone just before the IGVs. This can be explained by considering the overall trajectories of the injected droplets. With reference to Fig. 8, all the droplets injected by Inj2–Inj11 end up accumulating in the lower region for the present injection configuration. This behavior is well highlighted in Fig. 15, where the normalized accumulated energy variation among the rotor blades is shown after being averaged on the whole operating life of the machine. In the bottom rotor blades, the highest value of the accumulated energy due to washing droplets impacts was found.

Because of the shape of the compressor inlet case taking air from the top (as shown in Fig. 7), the airflow is forced to a sudden deviation to enter the machine axially. Because of this strongly non-symmetric flow, most of the water injected from the nozzles is pushed toward the bottom of the machine, and then enters the rotor close to the hub region (Fig. 16).

The earlier considerations help in explaining the erosion patterns shown for the bottom rotor blades along the three mesh evolution steps in Figs. 17 and 18, for the suction and the pressure sides, respectively. At the end of the simulation workflow, the peak of the erosion was found at the root of leading edge of rot08, as highlighted in the zoom-in added to Fig. 17. The maximum erosion increases at each evolution step of a constant value (i.e., e_{thr}), up to the assumed maximum erosion (e_{stop}), that in the present study is considered equal to 0.3 mm. The surface affected by erosion varies and increases as well as the value of the peaks. All the rotor leading edges are clearly subject to erosion but also some
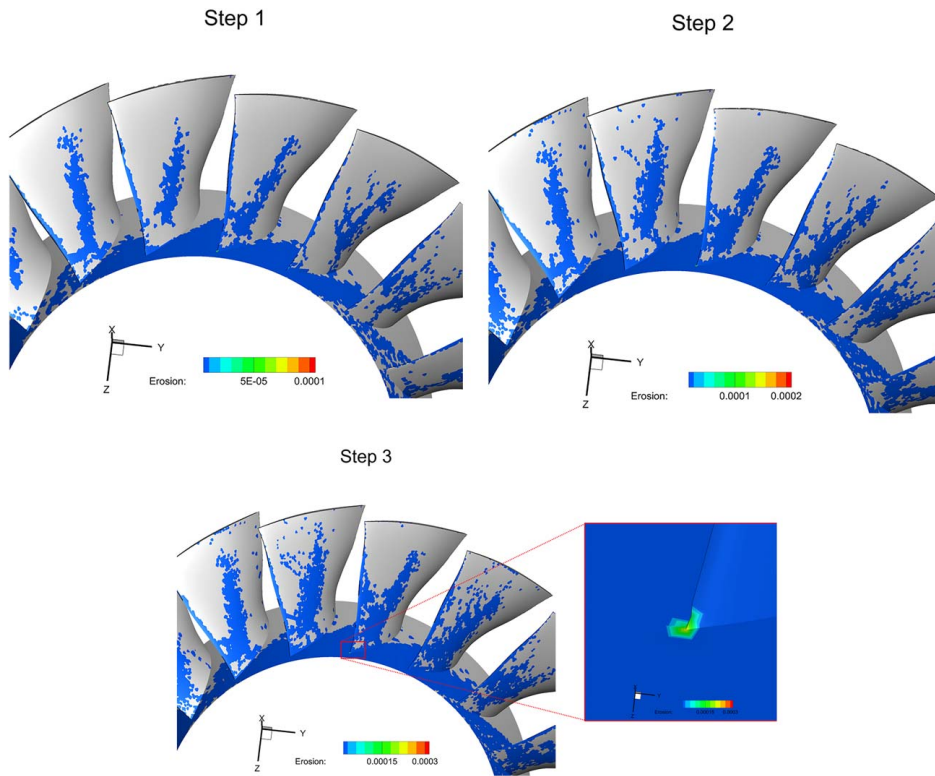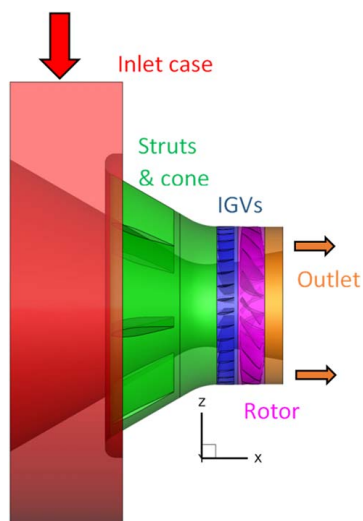
Fig. 17 Erosion evolution on the suction sides of some of the rotor blades (from left to right: rot12 to rot06 - see Fig. 8 for blade numbering). (© 2022 Baker Hughes Company–All rights reserved.)
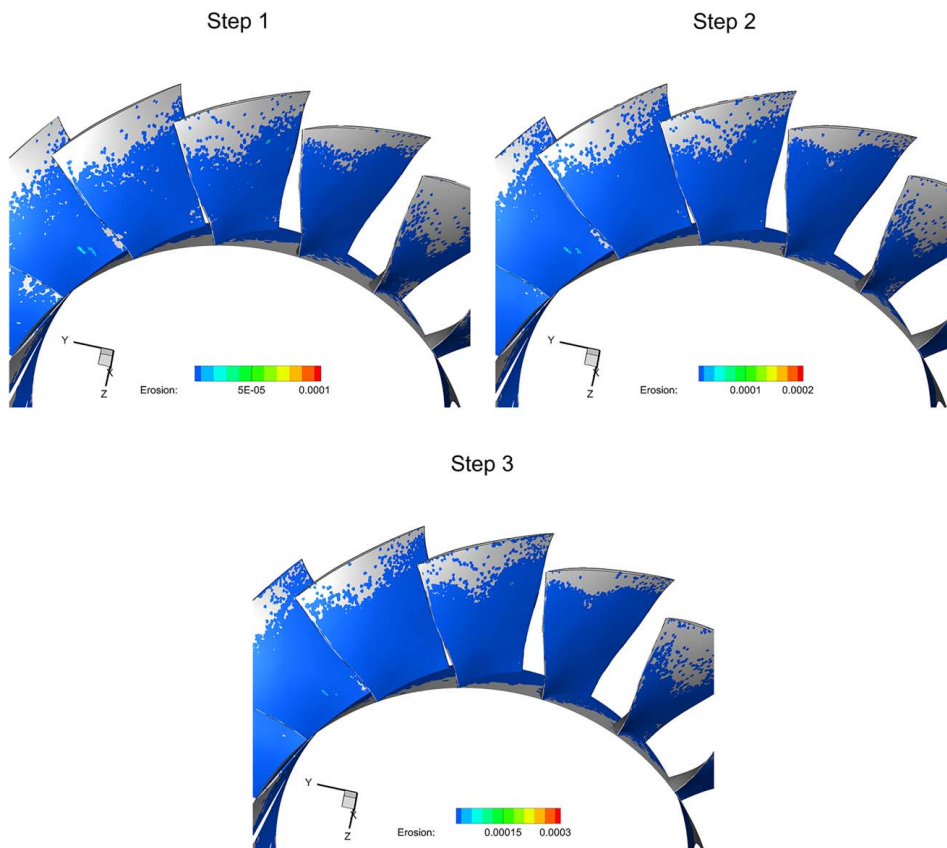
Fig. 18 Erosion evolution on the pressure sides of rotor blades (from left to right: rot12 to rot06–see Fig. 8 for blade numbering). (© 2022 Baker Hughes Company–All rights reserved.)
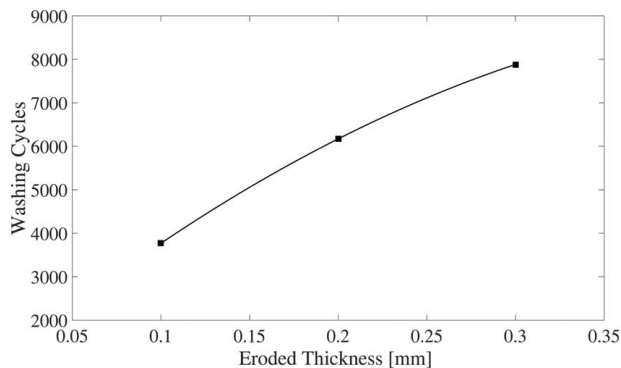
Fig. 19 Life prediction curve in terms of eroded thickness and water washing cycles.

Fig. 21 WTS time evolution in the domain subzones.

Fig. 20 Zones of the numerical domains.

Fig. 22 LIF time evolution in the domain subzones.

regions on the suction sides experience material removal due to droplet impacts. These regions are hit by the bigger droplets, which are characterized by higher inertia and are less prone to respond to the carrier fluid deviation due to the rotation. However, most of the impacts are observed on the pressure sides of the rotor blades (Fig. 18). At the end of the evolution steps, rotor pressure sides are completely eroded but the tip of the blades.
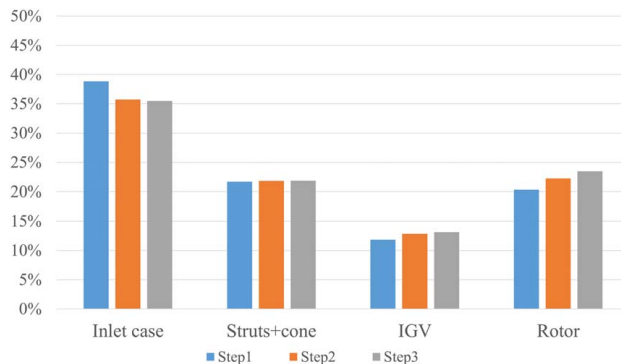
The scaling process based on the procedure explained in Sec. 2.4, permits to compute the life of the machine in terms of injected water mass needed to reach the maximum acceptable erosion value. Here, the graph shown in Fig. 19 is reported as a function of the number of washing cycles.

As expected, the time needed to overcome the successive evolution step decreases during the machine's operating life. This can be explained as follows: after the first simulation ends, in all the points where enough droplets have been impacted, the incubation period has already passed. Any new collision will result in an instantaneous (i.e., without an incubation period) material removal; the erosion peak will be higher resulting in a smaller life predicted.
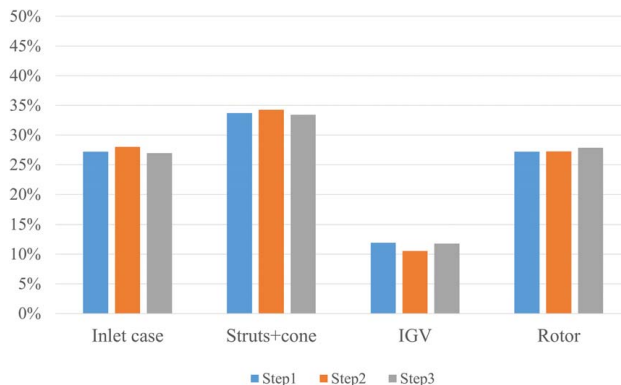
4.3 Time Evolution of Water Washing Efficiency Indices.
WWE was evaluated by means of the indices introduced in Sec. 2.2. First, the domain is divided into subzones as illustrated in Fig. 20.

Figure 21 shows the WTS variation with the evolution steps in all the domain subzones. Passing from step 1 to step 3, WTS results in

a slight decrease in the inlet case, from 39% to 36%, showing an asymptotic trend toward the latter value. It is worth noticing that a slight variation in the results can be due to a certain degree of randomness in the starting injection points of the droplets; this adds to the effect of grid variation (especially on the internal cone surface). WTS in the struts and cone region is about constant while a slight increase (about 1.3%) is predicted in the IGVs zone. Prediction in the rotor region also shows an increasing trend for the WTS index, going from 20.3% to 23.5%, which seems to be close to the maximum value reachable in this zone.

LIF time evolution is reported in Fig. 22. Some variations of this index are observed in the domain regions, but differences are limited to not more than 1%; therefore, grid modifications seem to have a negligible effect on how globally the impacted water mass divides among the domain subzones. However, the impact conditions may (even slightly) change, thus provoking different erosion on the surface, as shown in Sec. 4.2.

It is important to underline those indices in the rotor region as reported in Figs. 21 and 22 are global indices, thus summing the values predicted on all the rotor blades. This gives us an indication of how the water droplets distribute over the whole domain, but for a better prediction of the phenomenon, it is important to recall that in this work the frozen rotor approach is adopted. Indeed, in real operating conditions, all the blades are invested in the same amount of water and the wet surface should be uniform. For this reason, the blade having the maximum WTS is assumed to be representative of all the rotor blades (i.e., during rotation all the blades cross the region where maximum WTS is predicted), showing the behavior (as a function of the evolution steps) reported in Fig. 23. Passing from 1st step to 3rd step, WTS changes ranging between 47% and 49%. This variation, besides the effect of the randomness of the injection, can be due to the slight geometry variations predicted on the whole domain.
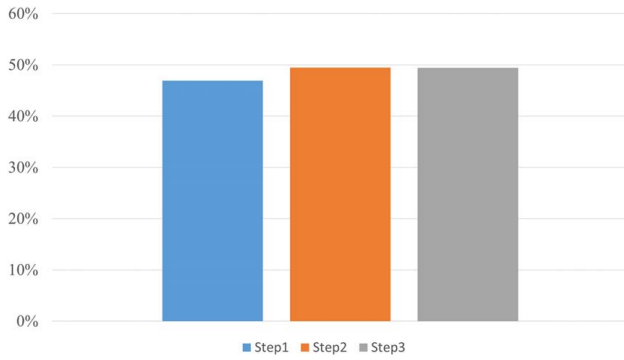
Fig. 23 Time evolution of maximum WTS among the rotor blades. (© 2022 Baker Hughes Company–All rights reserved.)

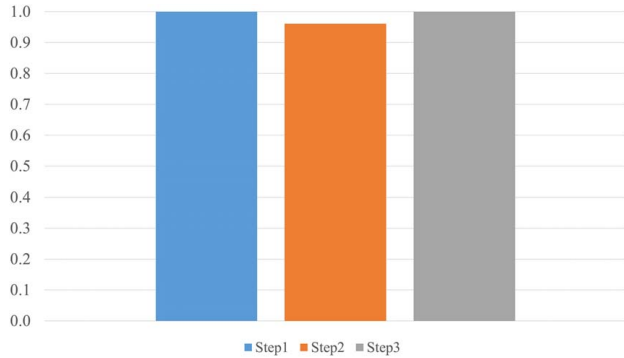**Fig. 24 Time evolution of the IMWS index. (© 2022 Baker Hughes Company–All rights reserved.)**

Time evolution of IMWS on the rotor blade showing the maximum wet surface is reported in Fig. 24. As reported in its definition, IMWS is computed by summing up the whole water mass hitting a rotor blade and then dividing it by the maximum wet surface. This index shows slight variations. Since maximum WTS increases with time, this means that water mass hitting the rotor blades also increases with time. The last two indices indicate that the considered grid variations provoke small effects on the global water washing efficiency. This behavior was somehow expected. In fact, the presented indices are integral values on large compressor regions, and the small local mesh modifications imposed were not supposed to alter significantly the overall washing efficiency behavior. However, erosive phenomena were proved to evolve nonlinearly during the compressor predicted life motivating the rationale of the present study.

5 Conclusion

A new approach for treating water washing erosion on compressor blades is reported. The developed model couples a semi-empirical water erosion model with a mesh morphing scheme to simulate the evolution of a real blade geometry, thus allowing to potentially assess the aerodynamic losses, the structural issues as well as the washing efficiency in the long-term washing process.

Here, a three-step erosion process is considered by evaluating the growth of erosions and the washing efficiency during the whole operating lifetime of the compressor. Some final remarks can be given as follows:

(a) The reported results showed that the growth of the erosion process must be considered while computing fluid flow and evaluating washing effectiveness.
(b) Erosion phenomena are observed in all the compressor regions, especially in the rotor where erosion peaks are reached at the hub of the leading edge.

(c) On the rotor blades, the eroded regions enlarge in time as well as the found peaks.
(d) The proposed procedure permits to predict the quantity of water mass injected before reaching a defined value of erosion in the rotor.
(e) The effectiveness of the washing procedure should be evaluated by using a set of properly defined indices able to take into account the effectiveness of the washing procedure in terms of extension of the wetted surfaces, fraction of water mass impacting all the machine regions, and the rotor blades.
(f) Such a procedure can give significant insights into the effectiveness of the adopted injectors configuration in terms of their number and position.
(g) Some of the selected indices slightly change as the erosion progresses, showing an increase in the wet surface on the rotor blades while the amount of water hitting the blades remains almost constant. This may lead to a reduction of the WWE because less water is washing the unit surface.

Further analyses are required to better clarify the influence of surface blade evolution on the profile losses, as well as on the blade structural strength. The liquid wall film motion on the compressor surfaces will also be an object of future investigations.

Conflict of Interest

There are no conflicts of interest.

Data Availability Statement

The datasets generated and supporting the findings of this article are obtainable from the corresponding author upon reasonable request.

Nomenclature

$$
\begin{aligned}
d &= \text{droplet diameter} \\
v &= \text{droplet impact velocity} \\
D &= \text{wavelength} \\
E &= \text{splashing parameter} \\
F &= \text{scaling factor} \\
h_0 &= \text{initial film thickness} \\
v_{cr} &= \text{droplet critical velocity} \\
v_{ref} &= \text{erosion model constant} \\
x_n &= \text{non-scaled node displacement} \\
C_r &= \text{roughness coefficient} \\
E_{inc} &= \text{incubation Energy} \\
X_n &= \text{scaled node displacement} \\
a, b, c &= \text{erosion model constants} \\
g, h, k &= \text{erosion model constants} \\
Hv &= \text{Vikers hardness} \\
Ra &= \text{surface roughness} \\
Ra_{ref} &= \text{surface reference roughness} \\
Re &= \text{Reynolds number} \\
We &= \text{Weber number} \\
d_{ref}, \dot{m}_{ref} &= \text{erosion model constants} \\
\delta_{bl} &= \text{boundary layer thickness} \\
\rho &= \text{liquid density} \\
\sigma &= \text{liquid surface tension}
\end{aligned}
$$

Abbreviations

$$
\begin{aligned}
\text{IGV} &= \text{inlet guide vane} \\
\text{IMWS} &= \text{normalized impacted water mass per unit of wet surface} \\
\text{LIF} &= \text{local impacted water mass fraction} \\
\text{UDF} &= \text{user defined function} \\
\text{WAMF} &= \text{water-to-air mass fraction} \\
\text{WDE} &= \text{water droplet erosion} \\
\text{WTS} &= \text{water-to-total surface ratio} \\
\text{WWE} &= \text{water washing efficiency}
\end{aligned}
$$

References

[1] Aker, G. F., and Saravanamuttoo, H. I. H., 1989, "Predicting Gas Turbine Performance Degradation Due to Compressor Fouling Using Computer Simulation Technique," ASME J. Eng. Gas Turbine Power, 111(2), pp. 343–350.

[2] Meher-Homji, C. B., Chaker, M. A., and Motiwala, H. M., 2001, "Gas Turbine Performance Deterioration," Proceedings of 30th Turbomachinery Symposium, Texas A&M University, Turbomachinery Laboratories, pp. 139–175.

[3] Song, T. W., Sohn, J. L., Kim, T. S., Kim, J. H., and Ro, S. T., 2003, "An Improved Analytic Model to Predict Fouling Phenomena in the Axial Compressor of Gas Turbine Engines," Proceedings of the International Gas Turbines Congress, Paper No. IGTC2003Tokyo TS-095.

[4] Madsen, S., and Bakken, L. E., 2018, "Gas Turbine Fouling Off-Shore; Effective Online Water Wash Through High Water-to-Air Ratio," Proceedings of the ASME Turbo Expo 2018, Oslo, Norway, June 11–15.

[5] Dominizi, I., Gabriele, S., Serra, A., and Borello, D., 2020, "Comparative Life Cycle Assessment of Different Gas Turbine Axial Compressor Water Washing Systems," Proceedings of the ASME Turbo Expo 2020: Turbomachinery Technical Conference and Exposition. Volume 3: Ceramics; Coal, Biomass, Hydrogen, and Alternative Fuels, Virtual, Online, Sept. 21–25.

[6] Agbadede, R., Pilidis, P., Igie, U. L., and Allison, I., 2015, "Experimental and Theoretical Investigation of the Influence of Liquid Droplet Size on Effectiveness of Online Compressor Cleaning for Industrial Gas Turbines," J. Energy Inst., 88(4), pp. 414–424.

[7] Wang, L., Yan, Z., Long, F., Shi, X., and Tang, J., 2016, "Parametric Study of Online Aero-Engine Washing Systems," IEEE International Conference on Aircraft Utility Systems (AUS), Beijing, China, Oct. 10–12, pp. 273–277.

[8] Baikov, I. R., Suleimanov, A. M., Kuznetsova, M. I., Kitaev, S. V., and Kolotilov, Y. V., 2018, "Improvement of the Composition of Detergent Solutions for the Removal of Deposits on the Axial-Compressor Blades of Gas-Turbine Units," Polym. Sci. Ser. D, 11(1), pp. 82–85.

[9] Kloter, S., Ashford, N. F., and Fitchett, D. R., 2019, "Laboratory and On-Site Findings Demonstrating the Greater Effectiveness of Biphase Water-Based Compressor Cleaners Over Monophase Cleaners," Proceedings of the ASME Turbo Expo 2019, Phoenix, AZ, June 17–21.

[10] Igie, U., Diez-Gonzalez, P., Giraud, A., and Minervino, O., 2016, "Evaluating Gas Turbine Performance Using Machine-Generated Data: Quantifying Degradation and Impacts of Compressor Washing," ASME J. Eng. Gas Turbine Power, 138(12), p. 122601.

[11] Wang, L., Hu, J., Huo, J., Liu, Q., Wei, B., Tang, J., and Shi, X., 2018, "Study on the Cleaning Mechanism of the Fouling of the Compressor Blade," CSAA/IET International Conference on Aircraft Utility Systems (AUS 2018), Guiyang, China, June 19–22, pp. 1–5.

[12] Musa, G., Igie, U., Pilidis, P., and Gowon, S., 2017, "Economic Viability of On-Line Compressor Washing for Different Rated Capacity," Proceedings of the ASME Turbo Expo 2017 Volume 3, Charlotte, NC, June 26–30.

[13] Margolis, H., 1991, "US Navy On-Line Compressor Washing of Marine Gas Turbine Engines," Proceedings of the International Gas Turbine and Aeroengine Congress and Exposition., Orlando, FL, June 3–6.

[14] Oosting, J., Boonstra, K., De Haan, A., Van Der Vecht, D., Stalder, J. P., and Eicher, U., 2007, "Online Compressor Washing on Large Frame 9-FA Gas Turbines Erosion on RO Compressor Blade Leading Edge Field Performance With a Novel on Line Wash System," Proceedings of the ASME Turbo Expo 2007, Montreal, Canada, May 14–17, pp. 775–784.

[15] Andreoli, M., Gabriele, S., Venturini, P., and Borello, D., 2019, "New Model to Predict Water Droplets Erosion Based on Erosion Test Curves. Application to On-Line Water Washing of a Compressor," Proceedings of the ASME Turbo Expo 2019: Turbomachinery Technical Conference and Exposition. Volume 2D: Turbomachinery, Phoenix, AZ, June 17–21.

[16] Kirols, H. S., 2015, "Water Droplet Erosion: Influencing Parameters, Representation, and Comparisons," Master's thesis, Concordia University, Montreal, Canada.

[17] Seleznev, L. I., Ryzhenkov, V. A., and Mednikov, A. F., 2010, "Phenomenology of Erosion Wear of Constructional Steels and Alloys by Liquid Particles," Therm. Eng., 57(9), pp. 741–745.

[18] Venturini, P., Andreoli, M., Borello, D., Gabriele, S., and Rispoli, F., 2019, "Modelling of Water Droplets Erosion on a Subsonic Compressor Cascade," Flow Turbul. Combust., 103(4), pp. 1109–1125.

[19] Di Gruttola, F., Agati, G., Venturini, P., Borello, D., Rispoli, F., Gabriele, S., and Simone, D., 2020, "Numerical Study of Erosion Due to Online Water Washing in Axial Flow Compressors," Proceedings of the ASME Turbo Expo 2020: Turbomachinery Technical Conference and Exposition, Volume 2B: Turbomachinery, Virtual, Online, Sept. 21–25.

[20] Agati, G., Di Gruttola, F., Gabriele, S., Simone, D., Venturini, P., and Borello, D., 2020, "Water Washing of Axial Flow Compressors: Numerical Study on the Fate of Injected Droplets," E3S Web of Conferences, 197, 75th National ATI Congress—#7 Clean Energy for all (ATI 2020)., Rome, Italy, Sept. 15–16.

[21] Agati, G., Di Gruttola, F., Gabriele, S., Simone, D., Venturini, P., and Borello, D., 2021, "Evaluation of Water Washing Efficiency and Erosion Risk in an Axial Compressor for Different Water Injection Conditions," E3S Web of Conferences, 312, 76th Italian National Congress ATI (ATI 2021), Rome, Italy, Sept. 15–17.

[22] Bowen, C. P., Libertowski, N. D., Mortazavi, M., and Bons, J. P., 2018, "Modeling Deposition in Turbine Cooling Passages With Temperature Dependent Adhesion and Mesh Morphing," Proceedings of the ASME Turbo Expo 2018: Turbomachinery Technical Conference and Exposition. Volume 2D: Turbomachinery, Oslo, Norway, June 11–15.

[23] Forsyth, P., Gillespie, D., and McGilvray, M., 2017, "Development and Applications of a Coupled Particle Deposition Dynamic Mesh Morphing Approach for the Numerical Simulation of Gas Turbine Flows," Proceedings of the ASME Turbo Expo 2017: Turbomachinery Technical Conference and Exposition. Volume 2D: Turbomachinery, Charlotte, NC, June 26–30. Paper No. GT2017-63295.

[24] Cinelli, R., Maggiani, G., Gabriele, S., Castorrini, A., Agati, G., and Rispoli, F., 2020, "Structural Analysis of a Gas Turbine Axial Compressor Blade Eroded by Online Water Washing," Proceedings of ASME Turbo Expo 2020, Turbomachinery Technical Conference and Exposition, London, UK, Sept. 21–25.

[25] Castorrini, A., Venturini, P., Corsini, A., and Rispoli, F., 2019, "Numerical Simulation of the Blade Aging Process in an Induced Draft Fan Due to Long Time Exposition to Fly Ash Particles," ASME J. Eng. Gas Turbines Power, 141(1), p. 011025.

[26] Castorrini, A., Corsini, A., Rispoli, F., Venturini, P., Takizawa, K., and Tezduyar, T. E., 2019, "Computational Analysis of Performance Deterioration of a Wind Turbine Blade Strip Subjected to Environmental Erosion," Comput. Mech., 1(21), pp. 1133–1153.

[27] Castorrini, A., Corsini, A., Morabito, F., Rispoli, F., and Venturini, P., 2017, "Numerical Simulation With Adaptive Boundary Method for Predicting Time Evolution of Erosion Processes," ASME Turbo Expo 2017: Turbomachinery Technical Conference and Exposition, Charlotte, NC, June 26–30.

[28] Castorrini, A., Venturini, P., Corsini, A., Rispoli, F., Takizawa, K., and Tezduyar, T. E., 2020, "Computational Analysis of Particle-Laden-Airflow Erosion and Experimental Verification," Comput. Mech., 65, pp. 1549–1565.

[29] ANSYS, Inc., 2020, ANSYS Fluent Theory Guide, Release 2020 R2, ANSYS, Inc., Southpointe.

[30] Launder, B. E., and Spalding, D. B., 1974, "The Numerical Computation of Turbulent Flows," Comput. Methods Appl. Mech. Eng., 3(2), pp. 269–289.

[31] Yarin, A. L., 2006, "Drop Impact Dynamics: Splashing, Spreading, Receding, Bouncing," Annu. Rev. Fluid Mech., 38(1), pp. 159–192.

[32] Josserand, C., and Thoroddsen, S. T., 2016, "Drop Impact on a Solid Surface," Annu. Rev. Fluid Mech., 48(1), pp. 365–391.

[33] Stanton, D. W., and Rutland, C. J., 1998, "Multi-Dimensional Modeling of Thin Liquid Films and Spray-Wall Interactions Resulting From Impinging Sprays," Int. J. Heat Mass Transfer, 41(20), pp. 3037–3054.

[34] O'Rourke, P. J., and Amsden, A. A., 2000, "A Spray/Wall Interaction Submodel for the KIVA-3 Wall Film Model," SAE Technical Paper 2000-01-0271.

[35] Mundo, C., Sommerfeld, M., and Tropea, C., 1995, "Droplet-Wall Collisions: Experimental Studies of the Deformation and Breakup Process," Int. J. Multiphase Flow, 21(2), pp. 151–173.

[36] Yarin, A. L., and Weiss, D. A., 1995, "Impact of Drops on Solid Surfaces: Self-Similar Capillary Waves, and Splashing as a New Type of Kinematic Discontinuity," J. Fluid Mech., 283, pp. 141–173.

[37] Lee, B. E., Riu, K. J., Shin, S. H., and Kwon, S. B., 2003, "Development of a Water Droplet Erosion Model for Large Steam Turbine Blades," KSME Int. J., 17(1), pp. 114–121.

[38] Ahmad, M., Casey, M., and Sürken, N., 2009, "Experimental Assessment of Droplet Impact Erosion Resistance of Steam Turbine Blade Materials," Wear, 267(9–10), pp. 1605–1618.

[39] Agati, G., Borello, D., Di Gruttola, F., Venturini, P., Rispoli, F., Serena, G., and Simone, D., 2021, "Numerical Study of Droplet Erosion in the First-Stage Rotor of an Axial Flow Compressor," Proceedings of the ASME Turbo Expo 2021: Turbomachinery Technical Conference and Exposition. Volume 2B: Turbomachinery–Axial Flow Turbine Aerodynamics; Deposition, Erosion, Fouling, and Icing, Virtual, Online, June 7–11.